Materials & Design 234 (2023) 112318

Contents lists available at ScienceDirect

Materials & Design

journal homepage: www.elsevier.com/locate/matdes

Hierarchical porosity design enables highly recyclable and efficient Au/TiO_2 composite fibers for photodegradation of organic pollutants

Shiling Dong [a], George T. Tebbutt [a], Robert Millar [b], Nicole Grobert [a,b,*], Barbara M. Maciejewska [a,*]

[a] Department of Materials, University of Oxford, Parks Road, Oxford OX1 3PH, UK
[b] WAE Technologies Ltd, Grove, Wantage, Oxfordshire, OX12 0DQ, UK

ARTICLE INFO

Keywords:
TiO_2 fibers
Electrospinning
Hierarchical porous structures
Plasmonic photocatalysts
Water treatment

ABSTRACT

Titanium dioxide (TiO_2) nanomaterials are ideal for photocatalytic degradation of organic pollutants but remain infeasible for industrial and municipal wastewater treatment because they cannot simultaneously satisfy two essential criteria for practical application, *i.e.*, high performance and good recyclability. Here, we design and create hierarchically porous TiO_2 fibers by dual-polymer templating sol–gel electrospinning combined with precise control over crystallization. The produced fibers own unique interconnected macropores throughout the fiber body that enable significantly enhanced light absorption and unlimited mass transport, making them ideal hosts for anchoring plasmonic nanoparticles (NPs). The Au NP-coupled TiO_2 fibers have photocatalytic efficiencies up to 6.6 times higher than plain TiO_2 fibers, showing comparable ability as commercial P25 nanopowder in photodegrading methyl blue (MB) and achieving complete decomposition of methyl orange (MO) in 90 min while P25 degrades only 66% MO. Unlike P25 or anatase TiO_2 nanopowders that non-reversibly disperse/aggregate in water, our composite fibers can be recollected through natural sedimentation, and their superior performance remains for at least six cycles. This work offers a practical and feasible design for high-performance recyclable photocatalysts for industrial-scale water treatment.

1. Introduction

Developing more efficient and powerful water treatment techniques and procedures is paramount to addressing the global shortage of clean water [1]. Among various modern water treatment methods, photocatalytic degradation is the greenest and most sustainable as it uses photocatalysts to harness clean solar energy [2]. Titanium dioxide (TiO_2) is an ideal and robust photocatalytic material and its inherent limitations, *e.g.,* the relatively wide band gap and high electron-hole recombination rate, have been extensively addressed in the past decades [3,4]. However, until today, TiO_2 nanomaterials are infeasible for industrial or municipal water treatment facilities, one of the primary reasons being the difficulty in separating the catalyst from the catalyst water suspension [5]. For example, removing commercial TiO_2 nanopowders (*e.g.,* P25) from water costs more than the price of the material itself [6]. Even though expensive and time-consuming processes such as centrifugation, ultrafiltration, and phase separation methods could reclaim most photocatalysts [7–9], the obtained materials are agglomerated and their is photocatalytic activity is vastly [10].

To address the recycling issue of the powder photocatalysts, one solution is immobilizing or coating TiO_2 materials on recyclable substrates, such as polymer fiber membranes, carbon fibers, and wool fabrics [11–13]. However, the instability of the supporting material, the large amount of inaccessible TiO_2 surface sites, and the insufficient interface adhesion severely limit their purification efficiency [14]. Much effort has been directed toward developing one-dimensional (1D) TiO_2 materials with high-aspect-ratio 1D structures to minimize aggregation and enable easy removal from water suspensions. Among Besid various existing 1D structures available, TiO_2 fibers can be continuously produced by electrospinning - a powerful technique with an unbeatable capacity for mass production of high-quality fibers [15,16]. This robust and versatile process can generate doped TiO_2 fibers by simply incorporating additives into the spinning solution and altering the calcination atmosphere [17,18]. Electrospinning is also potent for creating nanostructured TiO_2 fibers by design, such as hollow fibers [19], multichannel hollow fibers [20], tube-in-tube fibers [21], and other

* Corresponding authors.
E-mail addresses: nicole.grobert@materials.ox.ac.uk (N. Grobert), barbara.maciejewska@materials.ox.ac.uk (B.M. Maciejewska).

https://doi.org/10.1016/j.matdes.2023.112318
Received 9 August 2023; Received in revised form 6 September 2023; Accepted 8 September 2023
Available online 9 September 2023

complex porous structures [22]. Nevertheless, a significant proportion of surface area of the nanostructured fibers comes from the micropores (<20 nm) and mesopores (2–50 nm) close to the fiber surface and inside the fiber body. When used in water treatment, the water cannot reach these reactive sites unless the fiber undergoes severe structural degradation. Even if some inner surface sites can be wetted, the limited mass transport significantly suppresses the reaction rate. In comparison, macropores (>50 nm) serve as diffusion channels and support the transport of substances [23]. However, inducing macropores into highly crystalized TiO_2 nanofibers causes severe structural fragility. Once agitated in water, the porous fibers break into short segments or single crystals, quickly losing all the advantages associated with the 1D geometry [24]. To solve this dilemma, the new design of fiber materials is called, for example, porous microfibers that are more durable for recirculation and reuse and possess large surface areas for high efficiency.

Compositing TiO_2 fibers with other materials has been widely used to boost their photocatalytic performance. Coupling TiO_2 with plasmonic noble metal nanoparticles (NPs) has been proven the most successful because the Schottky junction formed at the metal NP/TiO_2 interface promotes the separation of photogenerated charge carriers, and the localized surface plasmon resonance (LSPR) effect of NPs significantly intensifies the local electric field and enhances light absorption [25–27]. However, these benefits can only be achieved with sophisticatedly designed semiconductor–metal NP architecture. Concerning fiber materials for water treatment applications, we propose four design principles: (i) NPs should be directly anchored onto TiO_2 instead of being suspended in water separately because the formation of Schottky junction requires direct metal NP/semiconductor contact [28], and the LSPR is limited to the very vicinity of NPs. (ii) NPs should be photostable without melting or irreversibly oxidized during photoreactions [29]. (iii) NPs should remain discrete and evenly distributed on the fiber surface without aggregation or agglomeration. (iv) The interaction between NPs and TiO_2 should be strong enough to avoid separation during recycling and reuse. To our knowledge, a TiO_2 fiber composite that meets all these criteria has not been fabricated yet.

Herein, we introduce our dedicatedly designed photocatalysts, plasmonic Au NP/hierarchical porous TiO_2 fibers (Au/HP-TiO_2). TiO_2 fibers with hierarchically porous structures are realized by a newly proposed method, dual-polymer templated sol–gel electrospinning. The co-existence of two types of pores significantly improves the ability of the fibre to captue and allows mass transport inside fiber structures. HP-TiO_2 is further coupled with Au NPs by a facile chemical reduction method, where varied-sized Au NPs are investigated for optimizing the plasmonic effects. The composite fibers are examined for photodegradation of several organic pollutants compared to the standard P25 TiO_2 nanopowder, and the superior recyclability of our composite fibers is highlighted. The outcomes of this work provide insights into designing and creating more economical and sustainable fiber materials for facilitating the utilization of photocatalysis technology in large-scale water treatment.

2. Materials and methods

2.1. Materials

Polyvinylpyrrolidone (PVP, M.W. 1,300,000), Titanium (IV) isopropoxide (TiP, ≥ 97 %), Tetraethoxysilane (TEOS, ≥ 99 %) were purchased from Alfa Aesar. Gold(III) chloride trihydrate, Copper(II) nitrate hemi(pentahydrate) ($Cu(NO_3)_2{\cdot}2.5\ H_2O$, ACS reagent, 98%), PTFE free flowing powder (mean size 1 μm), Ethanol (EtOH, ≥ 99.8% GC), Acetone (≥ 99.5% GC), Phenol (99.0–100.5% GC), and Titanium(IV) oxide anatase nanopowder (< 25 nm particle size, 99.7% trace metals basis) were purchased from Sigma-Aldrich. Acetic acid (AcOH) was purchased from Honeywell. Degussa P25 TiO_2 was acquired from Evonik (80:20 anatase:rutile). All reagents were used without further refinement.

2.2. Preparation of porous ceramic fibers

Spinning solutions containing dual-polymer templates were typically prepared by the following steps. 10 g PVP powder was dissolved in 100 mL EtOH to prepare a polymer stock solution. 5 mL TiP and 1.46 mL TEOS were mixed with 7.4 g PVP/EtOH solution (molar ratio TiP:TEOS = 2.5:1), yielding a yellowish solution (A). 0.225 g $Cu(NO_3)_2{\cdot}2.5\ H_2O$ was dissolved in 1 mL AcOH to give a clear blue solution (B). (B) was slowly added into (A), stirring at 65 °C for 3 h. For the fiber with 20 wt% PTFE loading, 0.62 g PTFE powder was gradually added into the solution, stirring vigorously and sonicating for 1 h. The amount of PTFE powder varied according to the loading level. The spinning solutions were fed into a syringe and electrospun using 20–25 kV (Genvolt High Voltage Power Supply). The nozzle-to-collector distance was 26 cm, and the extrusion rate was 5 mL h^{-1}. The temperature and humidity were 22 ± 3 °C and 45 ± 15 %, respectively. The collected TiO_2/PVP/PTFE and TiO_2/PVP precursor fibers were placed inside an alumina crucible (with lid) and heated in air at 10 °C/min ramping rate. Varied combinations of calcination temperatures and durations were examined.

2.3. Anchoring Au nanoparticles on TiO_2 fibers

Citrate-stabilized Au nanoparticles (NPs) were synthesized using a citrate reduction method according to the protocol developed by Frens *et al.* [30]. 25 mg TiO_2 fibers were dispersed in 50 mL $HAuCl_4$ solution (concentrations from 0.1 to 2 mM) warmed to 70–90 °C, stirred at 250 rpm for 30 min to allow $AuCl_4^-$ to fully adsorb on the fiber surface. The solution was heated to boiling while dropwisely adding 1 mL of freshly prepared 1 wt% sodium citrate solution. The solutions were boiled for an additional 15 min then cooled down to room temperature while stirring. Au/TiO_2 composite fibers were separated from Au NP solution by centrifugation at 500 rpm for 20 min, then carefully removing the supernatant. 50 mL of deionized water was refilled into the centrifuge tube, followed by a second round of centrifugation and supernatant removal. This process was repeated six times, finalized by washing the solid fiber acetone and drying at 70 °C for 4 h.

2.4. Materials characterization

Scanning electron (SEM) and scanning transmission electron microscopy (STEM) images were taken using a Zeiss Merlin. For SEM analysis, the samples were coated with 5 nm Pt. The fiber diameter and crystal size histograms were obtained by at least 200 unbiased counts of the fiber diameter from SEM images (coating thickness was included). Transmission electron microscopy (TEM) images were obtained by JEOL JEM-3000F operated at an acceleration voltage of 200 kV. Elemental maps were recorded using Energy-dispersive X-ray spectroscopy (EDS) (Oxford Instruments Inca).

Fourier transform infrared (FT-IR) attenuated total reflection (ATR) spectrum was recorded with a Varian Excalibur FTS 3500 FT-IR Spectrometer. Thermal gravimetry and differential thermal analysis (TG-DTA) were carried out on a Perkin Elmer TG/DTA 6300 instrument in dry air from room temperature to 1000 °C at 10 °C min^{-1} ramping rate. Brunauer-Emmett-Teller (BET) surface area analysis was performed based on N_2 adsorption isotherm obtained by a Micromeritics Gemini VII BET surface area analyzer. UV-vis diffuse reflectance spectroscopy (UV-vis DRS) was conducted on a Varian Carry 5000 UV-vis-NIR spectrophotometer using a Praying Mantis diffuse reflectance accessory. The powder samples were pressed into non-transparent flat pellets before characterization. All samples were characterized ensuring the same equipment calibration, and the results were presented without normalization. The optical band gaps of TiO_2 fibers and anatase TiO_2 nanopowder were determined by a Tauc plot method assuming indirect semiconductor, *i.e.*, by plotting $(\alpha h\nu)^{1/2}$ versus $h\nu$ and extrapolating the

linear tangent to the x-axis, where α is absorption coefficient, h is plank constant, and ν is the light frequency.

X-ray diffraction (XRD) patterns were obtained using a Bruker D8 Advance ECO diffractometer in a reflection mode at 40 kV and 25 mA using Cu Kα radiation (λ = 1.54 Å). Scherrer equation was used to determine the crystallite sizes

$$D = \frac{K\lambda}{\beta \times \cos\theta} \quad (1)$$

where D is the crystallite size, K (=0.9) is the crystallite-shape factor, β is full-width at half-maximum of diffraction peak, and θ is the Bragg angle in radians. The error bars were obtained by calculating the D from several diffraction peaks. The weight fraction of rutile (χ_{rutile}) was determined from [31]

$$\chi_{rutile} = (1 + \frac{0.8I_A}{I_R})^{-1} \quad (2)$$

where I_A and I_R are the peak intensities of anatase (1 0 1) and rutile (1 1 0), respectively

X-ray photoelectron spectroscopy (XPS) measurements were performed on a Thermo Scientific K-Alpha XPS with a microfocussed monochromated Al X-ray source. The source was operated at 12 keV, and the spot size was 400 μm. To compensate the effects of surface charging, the core-level spectra were referenced to the Si 2p peak at 102.8 eV (amorphous SiO_2). Shirley background and Lorentzian (LA) or Doniach Sunjic (DS) lineshape were used to fit the peak shape in CASA XPS software. Raman spectra were collected using a JY Horiba Labram Aramis imaging confocal microscope with a 532 nm green light laser. The laser intensity was tuned according to the Raman signal, *i.e.*, 25% for HP-TiO_2 and MP-TiO_2, decreased to 1% after loading Au NP due to the strong surface-enhanced spectroscopic effect [32]. Zeta potential was determined by a Malvern Zetasizer Nano ZS. HP-TiO_2, MP-TiO_2, and concentrated Au NP solutions were dispersed in 10 mM NaCl aqueous solution, slowly transferred to a folded capillary cell (DTS1060) and measured at 20 °C (room temperature) with six replicated measurements for each sample.

2.5. Finite-difference time-domain (FDTD) simulation

Ansys Lumerical 2023 R1 was used for conducting FDTD simulations. Two 3D models were built to simulate the light absorption of porous fibers. HP-TiO_2 fiber model, with an overall diameter of 822 nm, is composed of smooth TiO_2 spheres with 113 nm in diameter. The MP-TiO_2 fiber model is based on a rough cylinder with a roughness root-mean-square amplitude of 0.015 μm and correlation lengths in the ×, y planes and along z axis of 0.04 μm. Mesopores with 30–50 nm diameters and 300–500 nm lengths were etched from the fiber core. The composition of both fibers is TiO_2 (Siefke) according to the Lumerical database. The FDTD domain has perfectly matched layers (PML) boundary conditions at the × and y directions and periodical boundary conditions at the z direction, *i.e.,* along the fiber axis. The background medium was set to be either vacuum or water (Palik). The simulation time was 20 fs at 300 K. A mesh size of 4 nm with an accuracy level of 5 was used for the whole fiber structure. The incident angle of a 10-fs plane wave with a wavelength between 250 and 700 nm was kept at 90 degree to the surface of the fibers. An index monitor and a movie monitor were placed at one fiber cross-section to record the refractive index and electric field intensity. Four frequency-domain field and power monitors were placed in front of the four PML boundaries of the FDTD domain to monitor the reflection and transmission.

To investigate the plasmonic field-enhancement effect, periodic and symmetrical 3D models were built consisting of Au NPs-coated TiO_2 spheres. The diameters of the Au NPs were 10.5, 14.0, and 19.2 nm respectively. The source was a 534 nm laser light at normal incidence towards -z. The 2D electric field intensity distribution at the plane of Au NP/TiO_2 interfaces was monitored.

2.6. Photocatalytic activity and material recycling

The photodegradation of MB, MO, and phenol was evaluated at room temperature. In a typical experiment, 4.4 mg catalyst was added into 44 mL of 10 mg L^{-1} MB or MO aqueous solution. Dye solution was prepared and reserved in a 50 mL PTFE beaker to minimize the absorption of MB or MO on the beaker wall. The suspensions were stirred in the dark for 100 min to reach the adsorption–desorption equilibrium. 1.7 mL solution was withdrawn as a reference for the initial dye concentration (C_0). The solution was then illuminated with a 300 W xenon arc lamp (LOT-Oriel Instruments) operated at 130 W without any filter applied (UV–vis light: 260–800 nm). Since the light spot (diameter 5 cm) is larger than the beaker (diameter 3.8 cm), the actual irradiation intensity was approximately 75 W. Solutions were stirred throughout the photoreaction with air continuously bubbling into the solution. The temperature of the photodegradation measurement was controlled and kept between 22 and 30 °C. During the 90 min light irradiation, 1.8 mL solution was collected from the solution every 10 min and transferred into a 1.6 mL semi-micro polystyrene cuvette in the dark. The dispersions containing TiO_2 nanoparticles were centrifuged at 5000 rpm for 30 min before each measurement. The dye concentrations were examined by measuring the light absorbance using a Varian Carry 5000 UV–vis–NIR spectrophotometer. The characteristic peak intensities of MB and MO (664 and 464 nm) were converted into concentrations (C) using the pre-established calibration curves. Several blank experiments were conducted to examine the possible photolysis of MB and MO without photocatalyst or using Au NP as the sole photocatalyst; no decolorization was found in either case.

TiO_2-catalyzed photodegradation was analyzed using the Langmuir-Hinshelwood model, simplified to a first-order kinetics $\ln(C_0/C) = kt$, where k (min^{-1}) is the apparent reaction rate constant, and t (min) is the photodegradation time. The $\ln(C_0/C)$ versus t from 0 to 50 min was linearly fitted, and the slope of each fitting line was identified as the first-order rate constant k for each photocatalyst. Phenol degradation experiments were conducted following a similar procedure. 1 mg/10 mL catalyst was added into 80 ppm phenol aqueous solution (pH 7). The phenol concentration was measured every 20 min, tracing the characteristic 270 nm band. The UV-vis light source was equipped with a 400 nm long pass filter to evaluate the visible-light-driven photocatalytic activity.

For the recyclability test, 3 mg photocatalyst was dispersed in 30 mL of 10 mg L^{-1} MB or MO aqueous solution in a PTFE beaker. The dye concentration was monitored every 30 min. After photoreaction, the solution was left still in darkness for 2 h for the fibers to sediment and accumulate at the bottom of the beaker. P25 and anatase nanopowders were allowed to sediment overnight. The supernatant was carefully withdrawn from the beaker, and the rest of the solution was dried under 40–60 °C to reclaim the photocatalysts. Subsequently, 30 mL fresh MB or MO solution was added to the same beaker, and the measurement was repeated.

3. Results and discussion

3.1. Preparation of plasmonic composite fiber photocatalysts

Fig. 1**a** illustrates the synthetic process of plasmonic Au/TiO_2 -composite fibers. The innovative solution design in this work lies in the usage of 'dual-polymer templates', *i.e.,* polyvinylpyrrolidone (PVP) and polytetrafluoroethylene powder (PTFE), combined with the classic sol–gel electrospinning. PVP was pre-dissolved in ethanol and well-mixed with sol–gel reactants, playing the role of 'soft template' to support the continuous fiber structure [33]. PTFE powder is insoluble and nonreactive with the solution components, which preserves the shape in the precursor fiber and acts as a 'hard template' (Figure S1-S3). Our

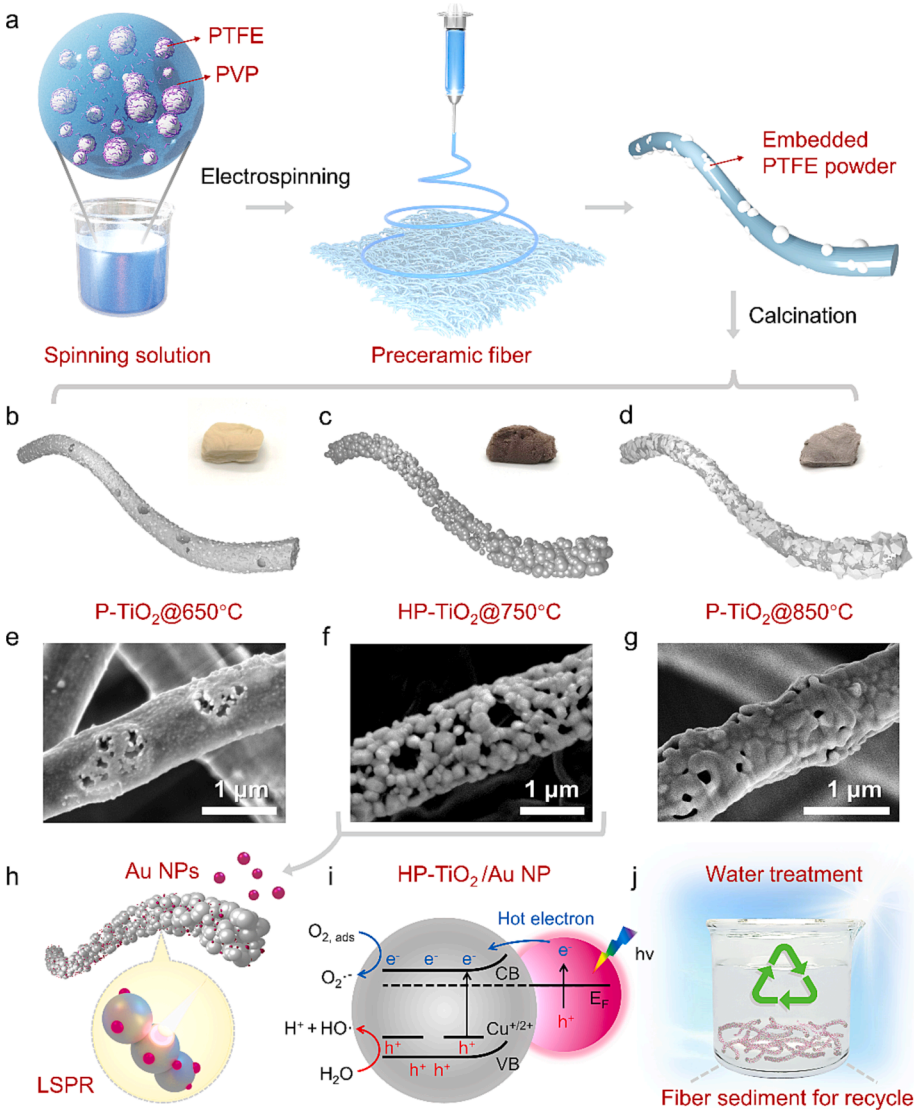

Fig. 1. Design and fabrication of hierarchically porous TiO_2 fibers (HP-TiO_2) coupled with plasmonic Au nanoparticles (Au NPs). (a) Scheme of the dual-polymer templated sol-gel electrospinning. Schematics, digital photos, and SEM images of the porous TiO_2 fibers (P-TiO_2) after calcining the precursor fibers at 650, 750, and 850 °C respectively, which are (b, e) P-TiO_2@650 °C, (c, f) HP-TiO_2@750 °C, and (d, g) P-TiO_2@850 °C. (h) HP-TiO_2 is coupled with plasmonic Au NPs via a citrate reduction method [41]. Under irradiation, the LSPR effect of Au NPs vastly enhances the local electric field and visible light absorption. (i) The mechanism of the photodegradation process of Au/HP-TiO_2 composite fiber, highlighting the plasmon-induced hot electrons transfer. The electrons (e^-) in the conduction band (CB) and the positive hole ($h^{\pm}$) in the valence band (VB) react with O_2 and H_2O to generate reactive radical species such as O^{2-}· and HO·, which effectively degrade organic species in water. (j) Schematic illustration shows that the composite fibers can naturally sediment and be easily collected for recycling.

designed spinning solution also contains titanium isopropoxide (TiP), copper nitrate hydrate, and tetraethyl orthosilicate (TEOS). Cu salt induces Cu dopants into the TiO_2 lattice, which are expected to reduce the band gap and create more reactive sites on the fiber surface [34,35]. TEOS plays three critical roles (Figure S4): (i) forming an amorphous SiO_2 layer surrounding the TiO_2 crystals, which connects the brittle TiO_2 crystals and helps in maintaining the continuous fiber structure [36]. (ii) The amorphous SiO_2 suppresses the atom diffusion between TiO_2 crystals and effectively retards the anatase-to-rutile phase transition [37,38]. (iii) TEOS induces phase separation within the spinning solution, leading to a mesoporous fiber structure [39,40].

Calcinating the precursor fiber at the relatively low temperature of 650 °C results in a macroporous fiber (P-TiO_2@650 °C) (Fig. 1**b, e**), which is yellow because the Cu dopants narrow the band gap. The macropores with geometry conformal to PTFE powders are direct evidence of the thermal decomposition of the hard template. The roughness on the fiber surface is attributed to the anatase TiO_2 nanocrystallites embedded in the amorphous matrix (Figure S5). Interestingly, calcination at 750 °C generates HP-TiO_2 fiber with two types of pores: PTFE-templated macropores with 200–500 nm in diameter and interconnected pores throughout the fiber body with a mean size between 40 and 80 nm measured as the distance between crystals (Fig. 1**c**, **f**). HP-TiO_2 appears dark brown due to the substantial open pores at the fiber surface, and such macropores are interconnected throughout the core of the fiber body, providing light-capturing cavities. Further increasing the calcination temperature to 850 °C promotes crystal growth, crystal coarsening, and anatase-to-rutile phase transition, which diminishes the hierarchically porous structure and results in grey-yellow P-TiO_2@850 °C (Fig. 1**d, g**).

Aiming at creating high-performance plasmonic photocatalysts, Au NPs were anchored on the surface of HP-TiO_2 (Fig. 1**h**). The LSPR of Au NP significantly amplifies the local electric field, resulting in improved visible light absorption and injection of highly energetic hot electrons to the conduction band (CB) of the semiconductor [42]. The CB of TiO_2 bends downwardly to align with the Fermi energy levels of metal NPs, *i.e.*, forming a Schottky junction [43], as illustrated in Fig. 1**i.** The Schottky junction builds an internal electric field inside TiO_2, which triggers the photogenerated electrons and holes to move in dissimilar directions, *i.e.,* promoting charge separation [28]. During water treatment, the electrons in the CB of TiO_2 react with adsorbed O_2 to generate superoxide radicals (•O^{2-}), and the photogenerated holes react with water to produce highly reactive hydroxyl radicals (•OH). Radicals and holes decompose the organic pollutant species pollutants into various intermediates and finally decompose them into inorganic species [3]. Moreover, because the composite fibers exhibit high-aspect-ratios with sub-micron diameters, they naturally sediment to the bottom of the

reactor and assemble without agglomeration (Fig. 1**j**). Therefore, such photocatalysts can be easily recycled after each use, leaving no hazardous substance in the treated water.

3.2. Dual-polymer templating method for hierarchical porosity

To explore the formation mechanisms of hierarchically porous structures, we prepared two spinning solutions, one with dual-polymer templates and another with PVP only, and electrospun them into TiO_2/PVP/PTFE and TiO_2/PVP precursor fibers. The former is calcined into HP-TiO_2 with an average fiber diameter of 822 nm and a crystal size of 108 nm (Fig. 2**a, b**, Figure S6). Under identical calcination conditions, TiO_2/PVP precursor fibers convert into mesoporous TiO_2 fibers (MP-TiO_2) with channel-shaped inner pores (Fig. 2**c, d**). The thermal decomposition of precursor fibers was studied using simultaneous TG-DTA (Fig. 2**e, f**). Moisture and residue solvents are removed at around 100 °C, PVP side substituents are eliminated between 300 and 352 °C, and the PVP carbon backbone cleaves at 352 to 425 °C [44]. TiO_2/PVP/PTFE show a further weight loss between 425 and 485 °C attributed to the decomposition of PTFE powder, confirmed by the sharp endothermic peak in the DTA curve [45]. Both precursor fibers have no noticeable weight loss above 500 °C, suggesting complete decomposition of organic components.

The microstructure of TiO_2 fibers was characterized by XRD, Raman, and nitrogen adsorption–desorption isotherms. HP-TiO_2 is well-crystalized, possessing 75 wt% anatase and 25 wt% rutile (JCPDS Card no. 21–1272 and 86–0148) (Fig. 2**g**). Similar to P25 Evonik (formerly Degussa), such a ratio is proven beneficial to photocatalytic activity because of the synergistic effects of anatase and rutile phases when they are in close contact [46,47]. MP-TiO_2 is highly amorphous, consisting of TiO_2 nanocrystallites in mixed anatase and rutile phases. Raman spectra agree with the XRD results, where HP-TiO_2 has sharp Raman peaks matching the anatase TiO_2, and MP-TiO_2 displays weak and broad bands indicating lower crystallinity (Figure S7). Both fibers with 4 mol% Cu show no evident CuO_x phase and no clear shift of the anatase and rutile peak. This supports the substitutional doping of Cu in TiO_2 lattice because Cu^{2+} (86 pm) with a similar ionic radius as Ti^{4+} (74.5 pm) tends to dissolve into TiO_2 crystal without distorting the lattice structures [48].

HP-TiO_2 exhibits type II isotherms corresponding to macroporous materials, whereas MP-TiO_2 presents type IV isotherms with H1 hysteresis loop indicating narrow cylindrical mesopores (Fig. 2**h**) [50]. The surface area of HP-TiO_2 is 17.8 $m^2\ g^{-1}$, smaller than 28.7 $m^2\ g^{-1}$ of MP-TiO_2. However, the mesopores inside fibers are not directly exposed to water, so they cannot be effectively involved in photoreactions. The light reflectance of HP-TiO_2, MP-TiO_2, and P25 TiO_2 nanopowder is demonstrated in Fig. 2**i**. HP-TiO_2 shows remarkably high visible light absorption, matching its dark brown color (Fig. 1c). Given that the optical band gap of both TiO_2 fibers is approximately 2.9 eV, smaller than anatase TiO_2 (3.22 eV) and P25 (3.15 eV) due to Cu doping (Figure S8), the enhanced light absorption of HP-TiO_2 is attributed to the unique hierarchical structure rather than the change of the absorption coefficients. We postulate three advantages of the hierarchical porous fiber design: (i) macropores open at the outermost fiber surface can effectively capture the incident light. (ii) The macropores throughout the fiber body are light cavities that enhance and extend the light absorption to the visible range. (iii) The interconnected pores serve as channels for mass transport, so all fiber surfaces are directly exposed to pollutant

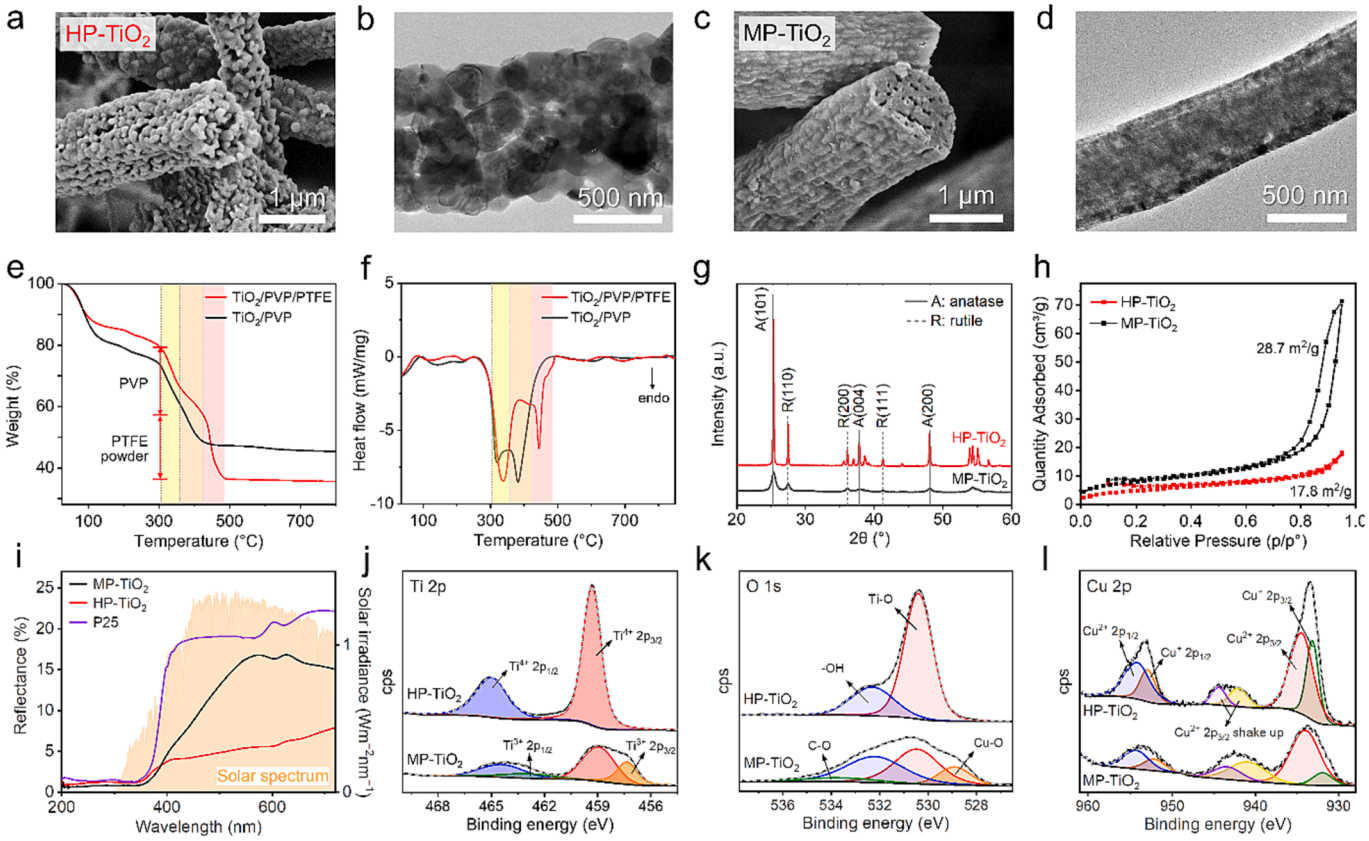

Fig. 2. Structural, compositional, and properties of porous TiO_2 fibers. SEM and TEM micrographs of (**a, b**) HP-TiO_2 and (**c, d**) MP-TiO_2 reveal their distinct porous fiber structures. (**e**) TG and (**f**) DTA of two precursor fibers indicate the stagewise thermal decomposition of PVP and PTFE. (**g**) XRD patterns and (**h**) N_2 adsorption–desorption isotherms of two porous TiO_2 fibers. (**i**) UV-vis diffuse reflectance spectra of TiO_2 fibers compared with the P25 TiO_2 nanopowder. The solar irradiance spectrum is plotted in the background [49]. XPS core level spectra of (**j**) Ti 2p, (**k**) O 1 s, and (**l**) Cu 2p. Each deconvoluted profile uses the same color code for the same bonding state.

species in the aqueous environment (which is verified by the attachment of Au NPs during solution synthesis).

XPS was used to characterize the chemical state/composition of TiO_2 fibers surface. The absence of F peaks suggests that the PTFE powders are entirely combusted, evacuating from the system as gaseous products with no evidence of F doping into the TiO_2 lattice (Figure S9). Ti 2p spectra indicate that HP-TiO_2 has Ti only in Ti^{4+} oxidation state at the surface, while MP-TiO_2 also contains Ti in the reduced Ti^{3+} form (Fig. 2**j**). O 1 s spectrum of HP-TiO_2 is deconvoluted into two components, O^{2-} in TiO_2 lattice, and –OH from surface hydroxyl groups and adsorbed water molecules (Fig. 2**k**). MP-TiO_2 has much higher –OH content and contains Cu-O and C-O components. Cu 2p spectra suggest the co-existence of $Cu^{\pm}$ and Cu^{2+} oxidation states at the surface of both fibers, and HP-TiO_2 possesses a higher $Cu^{\pm}/Cu^{2+}$ ratio (Fig. 2**l**). These differences in elemental composition and chemical states are explained by the different polycrystalline structures of the two materials. HP-TiO_2 consists of anatase and rutile TiO_2 crystals with stoichiometric Ti^{4+} and O^{2-} atoms, whereas MP-TiO_2 contains TiO_2 crystallites embedded in an amorphous matrix of Cu, Si, C, and O, *i.e.*, a non-stoichiometric solid solution with a variety of bonding coordination environments.

To understand the formation mechanism of the hierarchically porous structure, we traced the evolution of fiber morphology and crystalline structure during calcination (Fig. 3**a, b**, Figure S10). After 20 min calcination at 750 °C, anatase TiO_2 nanocrystallites form and embed in

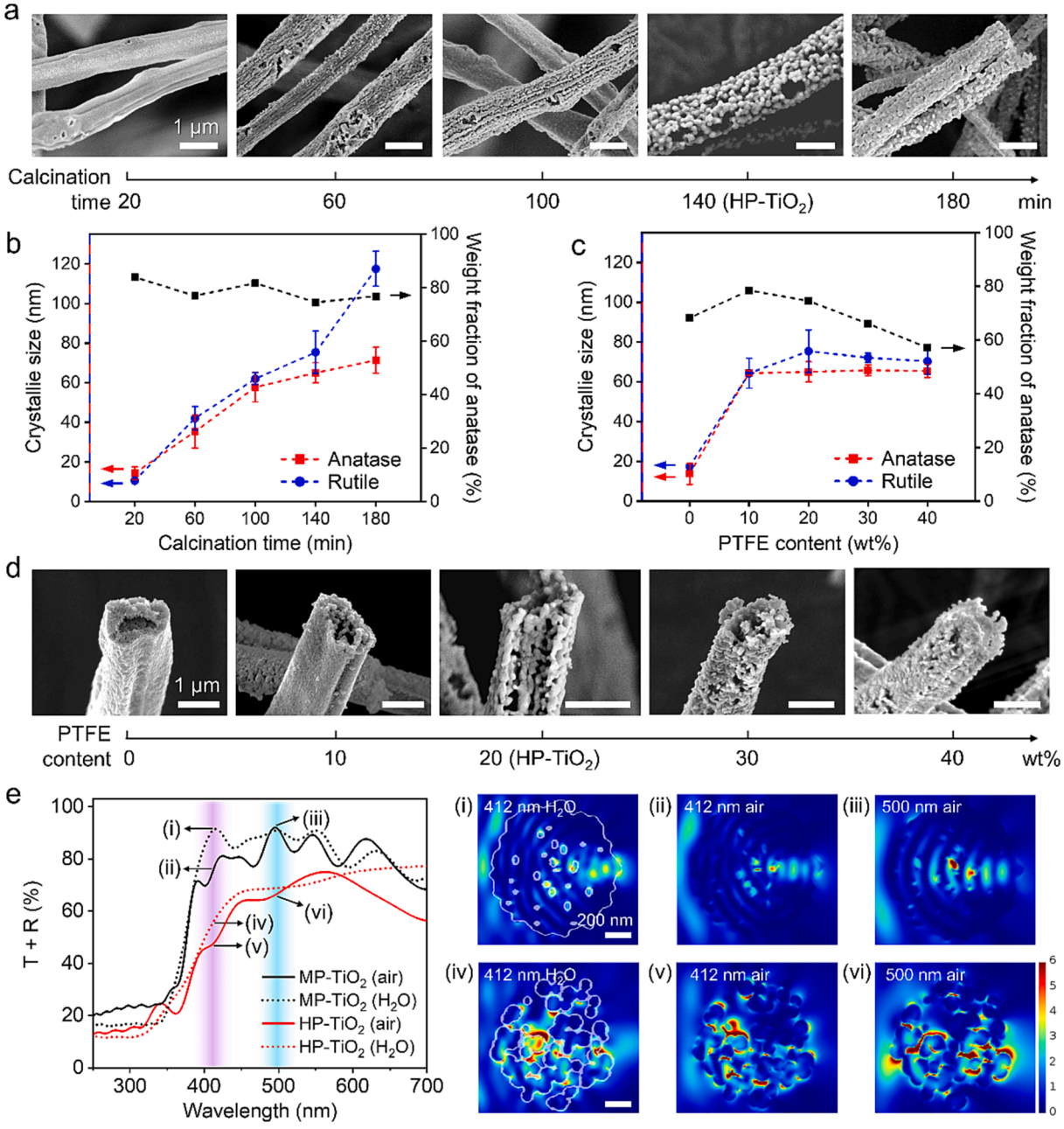

Fig. 3. Characterization of the evolution of the porous fiber structure. (**a**) SEM micrographs of TiO_2/PVP/PTFE precursor fiber calcined at 750 °C for varied durations. (**b**) Crystallite sizes and anatase weight fractions are plotted against the calcination time. (**c**) Structural information and (**d**) SEM images of precursor fibers with varied PTFE powder content (from 0 to 40 wt%) calcinated at 750 °C for 140 min. Scale bar in **a, d**: 1 μm. (**e**) Simulated optical spectra present the summation of the reflection (R) and transmission (T) of 3D fiber models from a normal incident plane wave. FDTD calculated electric field intensity distribution at the cross sections of (i-iii) HP-TiO_2 and (iv-vi) MP-TiO_2 fiber at 412 nm or 500 nm wavelength in air or water. The same scale bar and color scale are used in (i) - (vi). The outlines of fiber cross sections are superimposed on (i) and (iv).

the amorphous ceramic matrix. These nanocrystallites grow and merge into TiO_2 crystals between 60 and 100 min, creating a groovy pattern on the fiber surface. HP-TiO_2 appears at 140 min, consisting of bonded crystals as the solid skeleton and interconnected macropores inside the fiber. When the calcination time is extended to 180 min, the thermodynamically more stable rutile crystals rapidly increase in size by consuming the amorphous and small TiO_2 crystallites, diminishing the macropores and densifying the fiber structure [51].

The distinct morphology and significantly enhanced porosity of HP-TiO_2 are explained by a joint of Ostwald ripening and Kirkendall effect. Ostwald ripening refers to the growth of larger crystals or sol particles at the expense of the dissolution of small crystals or sol particles [52]. This process occurs during fiber calcination because the outer fiber surface is crystallized first and transformed into more stable crystalline phases, while the amorphous component (mainly at the fiber core) remains out of equilibrium and has higher solubility [53]. Upon increasing calcination time, the amorphous regions are progressively dissolved and depleted, generating cavities at the fiber interior. The Kirkendall effect refers to the phenomenon that when a net directional matter flows through an interface, an opposite vacancy flow compensates for the nonequilibrium diffusion and creates voids near the interface [54]. During the crystallization and crystal growth of TiO_2, Ti atoms directionally diffuse from the amorphous region to the crystal, leaving vacancy-generated micro-voids. Due to the high surface-to-volume ratio of nanoscale materials, the voids can easily reach the material boundary and coalesce with the others, forming the interconnected pores in HP-TiO_2. The amorphous component between TiO_2 crystals provides a fast transport path for surface diffusion [55].

The effects of PTFE loading level were also evaluated by varying the PTFE weight content from 0 to 40 wt%. 0 wt% PTFE gives MP-TiO_2, while 10 wt% PTFE generates macroporous TiO_2 fibers with higher crystallinity and larger crystallite sizes (Fig. 3**c, d**, Figure S11). This is because the thermal decomposition of PTFE exposes more inner surfaces of fibers and enables faster pyrolysis. Increasing PTFE loading to 20–40 wt% yields TiO_2 fibers with similar crystallite sizes but gradually reduced pore size and decreased anatase weight fraction. We postulate that the thermal decomposition of PTFE liberates gaseous products C_2F_2 that etches SiO_2 and leaches out the Si elements [45]. As a result, the residue amorphous SiO_2 is less effective in retarding TiO_2 crystal growth and phase transformation [38]. This is supported by the XPS elemental composition analysis, revealing the decrease of Si atomic percentage from 12.62 at% to 4.88 at% upon increasing PTFE content (Figure S12, Table S1).

TiO_2 fibers resulting from 20 to 40 wt% PTFE-loaded precursor fibers present enhanced visible light absorption compared to MP-TiO_2 (Figure S13). To explore the light-harvesting mechanisms, we built 3D models of HP-TiO_2 and MP-TiO_2 fibers for FDTD simulation (Figure S14, S15). A plane wave source with normal incidence was used, and the background material was either vacuum or water. The summation of reflection (R) and transmission (T) was plotted as a function of wavelength, and the absorption (A) is 1-R-T (Fig. 3**e**). The simulated spectra demonstrate that HP-TiO_2 has nearly doubled the light absorption in the visible light range, matching the experimental result. The oscillating feature of MP-TiO_2 spectra is due to the interference effect induced by the mesopores parallel to the fiber axis and the surface roughness. The total absorbed light remains similar in air and water, but the absorption peaks in water are red-shifted due to the decreased wavelength. To understand the reason behind the variation of the light absorption, we compared the electric field intensity distribution at the fiber cross sections in either vacuum or water at two chosen wavelengths: 412 nm, with significant absorption differences among the four simulation conditions (i, ii, iv, v); and 500 nm, with MP-TiO_2 showing an R + T peak and optical absorption 25% lower than HP-TiO_2 (iii, vi) (Fig. 3e, Figure S16, Movie S1-S4). It can be observed that light travels inside the HP-TiO_2 fiber through the open pores at the fiber surface, and intense fields appear in between the macropores. The interconnected macropores reflect and scatter light, thereby extending the optical path. Consequently, the maximum electric field intensity in the HP-TiO_2 model is approximately ten times higher than that of MP-TiO_2. It should be noted that this strategy of using pores to enhance light capture has mostly been adopted in substrate-supported photocatalyst design, *e.g.*, TiO_2 nanotube arrays [56], because they have tunable light depth penetration. Our HP-TiO_2 has similar benefits but can easily disperse in water, which makes it more effective and practical for harvesting solar irradiance energy.

3.3. Plasmonic Au/HP-TiO_2 composite fiber

Aiming to improve photocatalytic performance, we coupled the TiO_2 fibers with plasmonic Au NPs using a citrate reduction method, *i.e.*, Turkevich Method [41]. Au is chosen in our design due to their better chemical stability than Ag [29,57] and well-defined resonance peak compared to Pt [58]. During the synthesis, TiO_2 fibers were dispersed in 0.5, 1.0, and 1.5 mM $HAuCl_4$ solutions, and excessive sodium citrate was added to reduce $AuCl^{4-}$ into metallic Au under boiling conditions [41]. The as-obtained composite fibers are $Au_{0.5}$/HP-TiO_2, $Au_{1.0}$/HP-TiO_2, and $Au_{1.5}$/HP-TiO_2, respectively. Due to the porous structure, Au NPs are homogeneously distributed on both the outer and inner surface of HP-TiO_2 and remain well-separated (Fig. 4**a, b** and Figure S17). EDS mapping of Ti, O, Cu, and Au suggests that Cu is doped into TiO_2 lattice while Au NPs are attached to the TiO_2 fiber surface (Fig. 4**c**). The high-resolution TEM image in Fig. 4**d** displays that the chemically reduced Au NPs are polycrystalline with a hemispherical shape. The d-spacing on an Au NP is indexed as the (1 1 1) and (2 0 0) crystal planes of Au, and the lattice fringe on the fiber surface matches the (0 0 4) plane of anatase TiO_2. Comparing three Au/TiO_2 samples, both Au content and the average size of Au NPs increase with the $AuCl_4^-$ concentration, from 0.7 at% to 0.96 at%, and from 10.5 nm to 19.2 nm, respectively (Fig. 4**e** and Table S2). We additionally explored 0.1, 0.25, and 2 mM $HAuCl_4$ solutions for this synthesis, but the resultant Au NPs were too small to display any red color or underwent severe agglomeration.

The light-matter interaction of Au/HP-TiO_2 was investigated. The composite fibers have less visible light absorption than HP-TiO_2 due to the reflective nature of Au NPs, but the optical absorption thresholds remain the same, suggesting the band gap is unaltered (Fig. 4**f**). $Au_{1.0}$/HP-TiO_2 and $Au_{1.5}$/HP-TiO_2 show broad Au NP surface plasmon bands between 500 and 600 nm. The band position of $Au_{1.5}$/HP-TiO_2 is relatively red-shifted because of the larger NP size [59]. FDTD method was used to simulate the local electric field at the Au NP/TiO_2 interface under 543 nm laser excitation, *c.a.,* the LSPR absorption peak position of Au NPs (Fig. 4f inset, Figure S18, S19). A significant enhancement of the local field can be observed at the close interface of Au NP/TiO_2. With the diameter of Au NPs is increased from 10.5 to 14.0 and 19.2 nm, the highest electric field intensity is 5.1, 7.8, and 10.3 times respectively ci that in the bare TiO_2 crystals, respectively. This explains the Raman spectra of fibers shown in Fig. 4**g**, in which the excitation of surface plasmons results in 4 to 7 times amplifying the intensity of the prominent Raman peak, *i.e.,* E_g mode of anatase TiO_2 [32].

XPS was used to examine the surface composition and electronic structure of the Au/TiO_2 composite fibers. XPS spectra were aligned by calibrating the Si^{4+} 2p peak to 102.8 eV to remove any the charging effects on peak positions. As shown in Fig. 4**h**, anchoring Au NPs on the surface of TiO_2 results in a negative shift of Ti 2p binding energy by 0.48 eV, which indicates the electron transfer from Au NP to TiO_2. Fig. 4**i** suggests that three Au/TiO_2 materials have Au $4f_{7/2}$ and Au $4f_{5/2}$ binding energies of 84.0 eV and 87.7 eV, respectively, matching that of metallic Au [60]. Note that $Au_{0.5}$/HP-TiO_2 contains Au^{3+} at the surface attributed to the particle size effect, *i.e.*, Au^{3+} is more stable when the Au NPs are smaller [61,62]. Such unreduced Au^{3+} species and the large population of relatively small Au NPs (<6 nm) on $Au_{0.5}$/HP-TiO_2 explain why it shows an insignificant Au plasmon band despite having similar Au at% as the other composite fibers (Table S2).

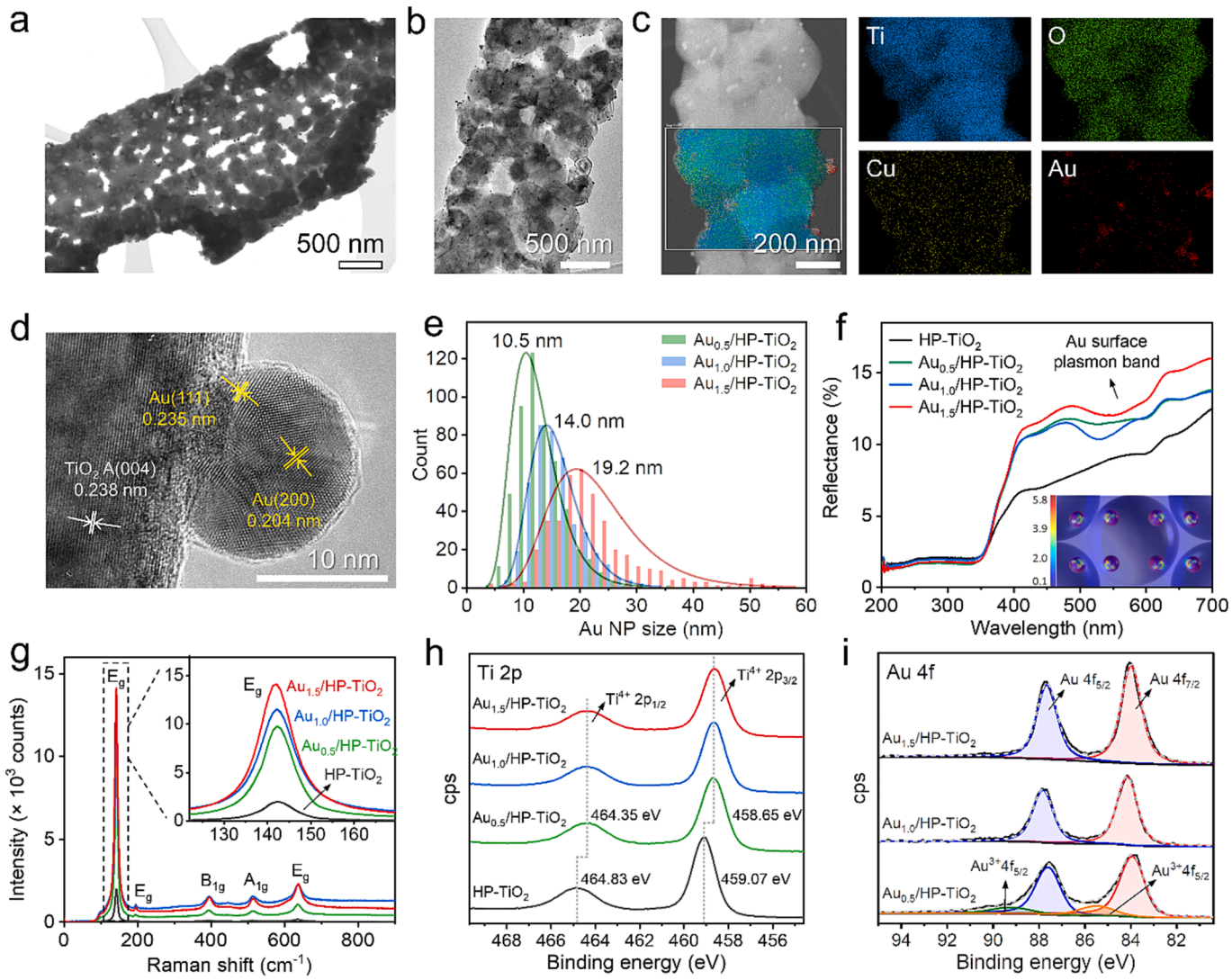

Fig. 4. Characterization and comparison of Au/HP-TiO_2 composite fibers. (**a**) STEM image, (**b**) TEM image, and (**c**) TEM/EDS elemental mapping on $Au_{1.5}$/HP-TiO_2. Color keys in (c): Ti (blue), O (green), Cu (yellow), and Au (red). (**d**) High-resolution TEM micrograph displays the interface between Au NP and anatase TiO_2. (**e**) Statistics of the NP size distribution. The average particle size in each sample is identified by fitting the histogram with a log-normal function. (**f**) Diffuse reflectance UV-vis spectra of HP-TiO_2 and Au/HP-TiO_2 fibers where the position of Au surface plasmon band is highlighted. Inset: Simulated electric field intensity distribution, displayed overlaid on the schematic of FDTD model, *i.e.*, 14 nm-diameter Au NPs attached to 113 nm-diameter TiO_2 particles. (**g**) Raman spectra of fiber samples recorded at 1% laser intensity. Inset: the most intense Raman peak for anatase TiO_2 (E_g). (**h**) Ti 2p XPS spectra show the shift of Ti^{4+} peak positions caused by Au NP attachment. (**i**) Deconvoluted Au 4f XPS spectra of Au/HP-TiO_2 composites. (For interpretation of the references to color in this figure legend, the reader is referred to the web version of this article.)

As the control, The same chemical reduction was used to deposit attach Au NPs on the surface of MP-TiO_2 as a controltha. Only very sparse Au NPs were attached regardless of the $HAuCl_4$ concentration (Figure S20). One reason is that the large number of –OH groups on the MP-TiO_2 surface results in a negative surface potential of −59.6 mV, more negative than HP-TiO_2 (-38.7 mV) (Figure S21). The strong electrostatic repulsion between MP-TiO_2 and $AuCl_4^-$ inhibits the adsorption of $AuCl_4^-$ on the fiber surface, preventing their nucleation into Au NP.

3.4. *Evaluation fo the Photocatalytic performance and recyclability evaluation*

We evaluated the photocatalytic activity of our composite fiber materials in the degradation of two types of model dyes, cationic methyl blue (MB) and anionic methyl orange (MO), and one colorless organic pollutant, phenol. Fig. 5**a** displays the color change of solutions when $Au_{1.0}$/HP-TiO_2 is used as the photocatalyst. The dye concentration was determined by measuring the UV–vis absorbance intensity at 664 cm^{-1} for MB and 464 cm^{-1} for MO (Fig. 5**b, c**). The photocatalytic performance of various TiO_2 fibers in decomposing MB is summarized in Fig. 5**d**, using commercial P25 as the reference material. All samples show neglectable dye adsorption before irradiation. After 90 min illumination, MP-TiO_2 decomposes 33.5 % of MB, and HP-TiO_2 removes 73 %. $Au_{1.0}$/HP-TiO_2 and $Au_{1.5}$/HP-TiO_2 have an initial photodegradation rate slower than P25 due to the smaller surface area, but both composite fibers can fully decompose MB within 80 min, which is as fast as P25. The plasmonic effects on improving the photocatalytic activity are significant in HP-TiO_2, yet it is minor for $Au_{1.5}$/MP-TiO_2 due to the insufficient surface attachment of Au NPs. The concentration profiles within the first 50 min are fitted using the Langmuir-Hinshelwood pseudo-first-order kinetics equation (Fig. 5**e**)

$$\ln\left(\frac{C_0}{C}\right) = kt \tag{3}$$

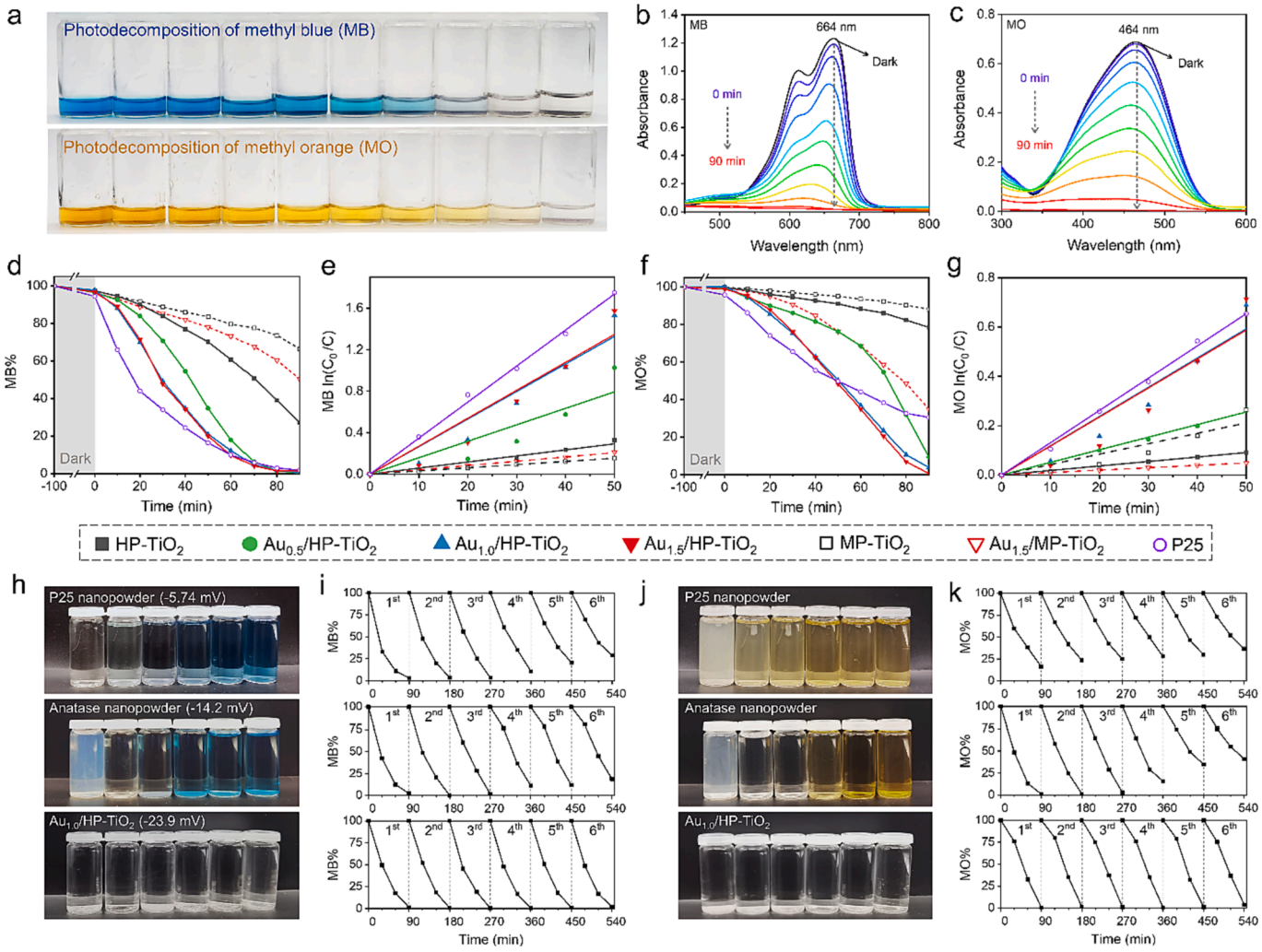

Fig. 5. Evaluation of the photocatalytic activities and recyclability of various TiO_2 materials. (**a**) Digital photos of the decolorization of MB and MO solutions catalyzed by $Au_{1.0}$/HP-TiO_2 at 10 min intervals. (**b, c**) UV-vis spectra of MB and MO solutions as a function of illumination time. The dye concentrations (C) are calculated based on the absorbance peak intensity at 664 nm and 464 nm, respectively. (**d, f**) The percentage of the residue dye as a function of irradiation time of various TiO_2 fibers compared with commercial P25. (**e, g**) Plots of $\ln(C_0/C)$ versus time, where C_0 is the dye concentration at 0 min, *i.e.*, after dark stir. The first 6 data points are linearly fitted to derive the first-order kinetic rate constant. The same legend is used in (**d-g**). (**h-k**) The recyclability test of P25 nanopowder, anatase TiO_2 nanopowder, and $Au_{1.0}$/HP-TiO_2 in this work (zeta potential value in brackets). After each photoreaction, the MB or MO solution containing photocatalyst is left for 2 h/overnight for fiber/nanopowder to fully sediment. The supernatant is collected as displayed in (**h, j**). The dye concentration percentage during photodegradation is monitored every 30 min (**i, k**).

where C_0 is the dye concentration after equilibrium absorption, C is the concentration at time t, and k is the rate constant [63,64]. The obtained k values and correlation coefficients (R^2) are listed in Table S3. $Au_{1.0}$/HP-TiO_2 and $Au_{1.5}$/HP-TiO_2 have significantly higher rate constants around 0.027 min^{-1}. The MB degradation rate using composite fibers is only 22 % lower than for P25 under UV light, despite its surface area of *ca.* 45–55 $m^2\ g^{-1}$ being three times higher than that of the composite fibers. TiO_2-catalyzed photodegradation of MB and MO is normally reported to follow the first-order kinetics for irradiation times < 60 min. P25, MP-TiO_2, and Au/MP-TiO_2 fit the first-order reaction profile with correlation coefficients $R^2 > 0.998$, whereas HP-TiO_2 and Au/HP-TiO_2 deviate from the Langmuir-Hinshelwood model. The reasons behind such deviations could be their dissimilar pathways in organic dye degradation, during which the generated intermediates modify the surface properties of TiO_2 fiber and regulate the reaction rate [65,66].

The plasmonic effects are also significant in the photodegradation of MO (Fig. 5**f, g**). MP-TiO_2 only removed 12 % MO ($k = 0.001\ min^{-1}$) in 90 min, while HP-TiO_2 reduced the amount of MO by 21.6 % ($k = 0.002\ min^{-1}$). $Au_{0.5}$/HP-TiO_2 presents 90.6 % degradation of MO within 90 min ($k = 0.005\ min^{-1}$), while $Au_{1.0}$/HP-TiO_2 and $Au_{1.5}$/HP-TiO_2 achieve full elimination ($k = 0.012\ min^{-1}$). The MO degradation rate of P25 is 9.2 % higher than composite fibers at the first 50 min, yet the rate decreases with time and leaves 34 % residue MO after 90 min irradiation. Overall, in our design, anchoring Au NPs at low surface loading of < 1 at% increases the dye degradation rate of HP-TiO_2 fiber up to 4.5 times for MB and 6.6 times for MO. In comparison, Yang *et al.* functionalized TiO_2 nanofibers by 4 wt% 10 nm-Au NPs and reported a 1.67 times improvement in the MB degradation rate [67]. Nalbandian *et al.* embedded Au NPs inside TiO_2 nanofibres and found that NPs offer no noticeable improvement, even deteriorating the photocatalytic performance at high loading levels [68]. Kochuveedu *et al.* decorated different sizes of Au NPs on SiO_2@TiO_2 spheres, observing that the enhancement of MB decomposition is significant when Au NPs have 15 nm in diameter and are loaded at a high number density of $> 700/\mu m^2$ [69]. Therefore, a rational design of the Au NP/TiO_2 configuration, as shown in this study, enables efficient enhancement of the photocatalytic efficiencies with lower Au content, *i.e.,* lower costs.

We also evaluated the photodegradation of colorless phenol in a

neutral aqueous solution using $Au_{1.0}$/HP-TiO_2 (Figure S22). $Au_{1.0}$/HP-TiO_2 and Degussa P25 exhibit 70 % and 79 % phenol removal under 120 min UV light irradiation. P25 possesses a higher reaction rate of 0.0089 min^{-1} versus 0.0068 min^{-1} of composite fiber due to the nanosized powder and larger specific surface area. The photodegradation was also tested under visible light by applying a 400 nm long-pass optical filter (Figure S23). HP-TiO_2 resulted in negligible MB degradation, while $Au_{1.0}$/HP-TiO_2 showed > 37 % MB reduction within 3 h. Although the decomposition rate of visible-light-driven photocatalysis is much lower, these results are in agreement with the conclusions of previous studies, suggesting that the attachment of plasmonic NPs contributes to photoactivity through two mechanisms: (i) enhancing visible light response through LSPR-induced light absorption and charge injection and (ii) improving the UV-light activity by forming Schottky barrier at the Au/TiO_2 interface that separates the charge carriers and increases their concentration and lifetime [68,70,71].

To tackle the poor recyclability of most nanostructured TiO_2 materials, we show that our fiber-based photocatalysts can be recycled by a straightforward sedimentation method, *i.e.*, leaving the solution to settle for 2 h, extracting the supernatant as purified water, and drying the remaining solution to restore the solid materials. As shown in Fig. 5**h-k**, the supernatants collected from $Au_{1.0}$/HP-TiO_2 solutions are colorless and transparent, suggesting that gravitational force is enough to drive the complete sedimentation of the photocatalyst. The recycled material also maintains high photocatalytic performance during six cycles. The XRD spectra and SEM images of the recycled Au/HP-TiO_2 show no observable change in the size and distribution of Au NPs, and no phase transformation or morphological change of the TiO_2 fibers (Figure S24, S25). Moreover, the fiber length was barely reduced after six cycles of vigorous stirring during photoreaction, proving the mechanical robustness of our composite fibers (Figure S26).

In contrast, commercial P25 nanopowder and anatase TiO_2 nanopowder (both with < 25 nm particle size) show evident loss of photocatalytic efficiency upon recycling, even though the sedimentation time has been extended overnight. This is ascribed to the loss of material and the aggregation of nanoparticles. As shown in the upper panels of Fig. 5h, 5j, the supernatants collected and removed from the first two cycles are translucent because the negatively charged TiO_2 nanoparticles form a relatively stable suspension. The supernatant of P25 in MB solution is clear, but it is because positive MB ions absorb onto the negative surface of P25 and increase the surface potential close to 0, which hugely destabilizes the primary particles and causes aggregation [72]. The anatase nanopowders, despite their more negative surface charge, also aggregate in the following recycling cycles and are further welded together (Figure S27). This morphology change severely reduces the number of active surface sites and causes the decline of photocatalytic activity upon recycling and reuse. Therefore, Au/TiO_2 composite fibers with excellent recyclability are more promising for long-term use in industrial and municipal water treatment facilities.

4. Conclusion

In this work, we reported the synthesis and characterization of a new photocatalyst material by design – hierarchical porous TiO_2 fibers (HP-TiO_2) decorated with plasmonic Au NPs. The distinct hierarchical porosity was created by combining the dual-polymer templating method with sol–gel electrospinning, which offers tremendous advantages in boosting light absorption and facilitating mass transport. HP-TiO_2 was subsequently coupled with plasmonic Au NPs of controlled sizes. The resulting Au/HP-TiO_2 composite microfibers show highly competitive photodegradation efficiency to P25 nanopowders in degrading MB and phenol, outperforming P25 in eliminating MO, and, more importantly, they are highly recyclable. Separating these fibers from water can be as simple as by natural sedimentation only, without any filtration or centrifugation step. The successful design and fabrication of such materials reveal the potential of fiber materials in aiding the transfer of photocatalytic technology from lab-scale to industrial water treatment.

CRediT authorship contribution statement

Shiling Dong: Conceptualization, Methodology, Investigation, Data curation, Writing – original draft, Visualization. **George T. Tebbutt:** Investigation, Data curation. **Robert Millar:** Project administration, Resources. **Nicole Grobert:** Writing – review & editing, Supervision, Project administration, Resources. **Barbara M. Maciejewska:** Conceptualization, Supervision.

Declaration of Competing Interest

The authors declare that they have no known competing financial interests or personal relationships that could have appeared to influence the work reported in this paper.

Data availability

Data will be made available on request.

Acknowledgments

The authors gratefully acknowledge the financial support from the Faraday Institution (B.M.M, N.G). We also acknowledge the microscopy and spectrometry support from Oxford Materials Characterization Service and David Cockayne Centre for Electron Microscopy, Department of Materials, University of Oxford, alongside financial support provided by the Henry Royce Institute (Grant ref EP/R010145/1). G.T.T acknowledges the EPSRC studentship 2439153, EP/T517811/1. N.G. thanks The Royal Society for the Royal Society Industry Fellowship.

Appendix A. Supplementary data

Supplementary data to this article can be found online at https://doi.org/10.1016/j.matdes.2023.112318.

References

[1] M.M. Mekonnen, A.Y. Hoekstra, Four billion people facing severe water scarcity, Sci. Adv. 2 (2016) e1500323.
[2] T. Velempini, E. Prabakaran, K. Pillay, Recent developments in the use of metal oxides for photocatalytic degradation of pharmaceutical pollutants in water—a review, Mater. Today Chem. 19 (2021), 100380.
[3] S.-Y. Lee, S.-J. Park, TiO2 photocatalyst for water treatment applications, J. Ind. Eng. Chem. 19 (2013) 1761–1769, https://doi.org/10.1016/j.jiec.2013.07.012.
[4] E.M. Bayan, L.E. Pustovaya, M.G. Volkova, Recent advances in TiO2-based materials for photocatalytic degradation of antibiotics in aqueous systems, Environ. Technol. Innov. 24 (2021), 101822.
[5] D. Cho, S.i. Chen, Y. Jeong, Y.L. Joo, Surface hydro-properties of electrospun fiber mats, Fibers Polym. 16 (7) (2015) 1578–1586.
[6] J. Tian, Z. Zhao, A. Kumar, R.I. Boughton, H. Liu, Recent progress in design, synthesis, and applications of one-dimensional TiO 2 nanostructured surface heterostructures: a review, Chem. Soc. Rev. 43 (20) (2014) 6920–6937.
[7] M.E. Fabiyi, R.L. Skelton, Photocatalytic mineralisation of methylene blue using buoyant TiO2-coated polystyrene beads, J. Photochem. Photobiol. A Chem. 132 (1-2) (2000) 121–128.
[8] H.O. Stancl, K. Hristovski, P. Westerhoff, Hexavalent chromium removal using UV-TiO2/ceramic membrane reactor, Environ. Eng. Sci. 32 (8) (2015) 676–683.
[9] P. Westerhoff, P. Alvarez, Q. Li, J. Gardea-Torresdey, J. Zimmerman, Overcoming implementation barriers for nanotechnology in drinking water treatment, Environ. Sci. Nano 3 (6) (2016) 1241–1253.
[10] J. Chen, F. Qiu, W. Xu, S. Cao, H. Zhu, Recent progress in enhancing photocatalytic efficiency of TiO2-based materials, Appl. Catal. A 495 (2015) 131–140, https://doi.org/10.1016/j.apcata.2015.02.013.
[11] Y. Zhang, W. Cao, B. Zhu, J. Cai, X. Li, J. Liu, Z. Chen, M. Li, L. Zhang, Fabrication of NH2-MIL-125(Ti) nanodots on carbon fiber/MoS2-based weavable photocatalysts for boosting the adsorption and photocatalytic performance, J. Colloid Interface Sci. 611 (2022) 706–717, https://doi.org/10.1016/j.jcis.2021.12.073.
[12] H. Zhai, Z. Liu, L. Xu, T. Liu, Y. Fan, L. Jin, R. Dong, Y. Yi, Y. Li, Waste textile reutilization via a scalable dyeing technology: a strategy to enhance dyestuffs degradation efficiency, Adv. Fiber Mater. 4 (2022) 1595–1608, https://doi.org/10.1007/s42765-022-00192-1.

[13] Y. Zhang, A. Sun, M. Xiong, D.K. Macharia, J. Liu, Z. Chen, M. Li, L. Zhang, TiO2/BiOI p-n junction-decorated carbon fibers as weavable photocatalyst with UV–vis photoresponsive for efficiently degrading various pollutants, Chem. Eng. J. 415 (2021), 129019, https://doi.org/10.1016/j.cej.2021.129019.

[14] H. Lv, Y. Liu, Y. Bai, H. Shi, W. Zhou, Y. Chen, Y. Liu, D.-G. Yu, Recent combinations of electrospinning with photocatalytic technology for treating polluted water, Catalysts 13 (2023) 758.

[15] W. Song, Y. Tang, C. Qian, B.J. Kim, Y. Liao, D.-G. Yu, Electrospinning spinneret: A bridge between the visible world and the invisible nanostructures, Innov. 4 (2023), 100381, https://doi.org/10.1016/j.xinn.2023.100381.

[16] L. Persano, A. Camposeo, C. Tekmen, D. Pisignano, Industrial upscaling of electrospinning and applications of polymer nanofibers: a review, Macromol. Mater. Eng. 298 (2013) 504–520, https://doi.org/10.1002/mame.201200290.

[17] J. Song, R. Guan, M. Xie, P. Dong, X. Yang, J. Zhang, Advances in electrospun TiO2 nanofibers: design, construction, and applications, Chem. Eng. J. 431 (2022) 134343.

[18] S.M. Pasini, A. Valerio, G. Yin, J. Wang, S.M.A.G.U. de Souza, D. Hotza, A.A.U. de Souza, An overview on nanostructured TiO2–containing fibers for photocatalytic degradation of organic pollutants in wastewater treatment, J. Water Process Eng. 40 (2021), 101827.

[19] D. Li, Y. Xia, Direct fabrication of composite and ceramic hollow nanofibers by electrospinning, Nano Lett. 4 (2004) 933–938, https://doi.org/10.1021/nl049590f.

[20] T. Zhao, Z. Liu, K. Nakata, S. Nishimoto, T. Murakami, Y. Zhao, L. Jiang, A. Fujishima, Multichannel TiO 2 hollow fibers with enhanced photocatalytic activity, J. Mater. Chem. 20 (2010) 5095–5099.

[21] L. Lang, D. Wu, Z. Xu, Controllable fabrication of TiO2 1D-nano/micro structures: solid, hollow, and tube-in-tube fibers by electrospinning and the photocatalytic performance, Chem. – A Eur. J. 18 (2012) 10661–10668, https://doi.org/10.1002/chem.201200378.

[22] B. Liu, L. Peng, Facile formation of mixed phase porous TiO2 nanotubes and enhanced visible-light photocatalytic activity, J. Alloy. Compd. 571 (2013) 145–152, https://doi.org/10.1016/j.jallcom.2013.03.221.

[23] Y. Chen, N. Wang, O. Ola, Y. Xia, Y. Zhu, Porous ceramics: Light in weight but heavy in energy and environment technologies, Mater. Sci. Eng. R Reports. 143 (2021), 100589, https://doi.org/10.1016/j.mser.2020.100589.

[24] W. Fu, W. Xu, K. Yin, X. Meng, Y. Wen, L. Peng, M. Tang, L. Sun, Y. Sun, Y. Dai, Flexible-in-rigid polycrystalline titanium nanofibers: a toughening strategy from a macro-scale to a molecular-scale, Mater. Horizons. 10 (2023) 65–74, https://doi.org/10.1039/D2MH01255C.

[25] R. Brisbin, J. Zhou, T. Bond, L. Voss, A.J. Simon, R. Baxter, A.S.P. Chang, Plasmonics-enhanced UV photocatalytic water purification, J. Phys. Chem. C 125 (18) (2021) 9730–9735.

[26] Y. Lu, H. Zhang, D. Fan, Z. Chen, X. Yang, Coupling solar-driven photothermal effect into photocatalysis for sustainable water treatment, J. Hazard. Mater. 423 (2022), 127128, https://doi.org/10.1016/j.jhazmat.2021.127128.

[27] W. Hou, S.B. Cronin, A review of surface plasmon resonance-enhanced photocatalysis, Adv. Funct. Mater. 23 (13) (2013) 1612–1619.

[28] X. Zhang, Y.L. Chen, R.-S. Liu, D.P. Tsai, Plasmonic photocatalysis, Reports Prog. Phys. 76 (4) (2013) 046401.

[29] K. Awazu, M. Fujimaki, C. Rockstuhl, J. Tominaga, H. Murakami, Y. Ohki, N. Yoshida, T. Watanabe, A plasmonic photocatalyst consisting of silver nanoparticles embedded in titanium dioxide, J. Am. Chem. Soc. 130 (2008) 1676–1680, https://doi.org/10.1021/ja076503n.

[30] G. Frens, Controlled nucleation for the regulation of the particle size in monodisperse gold suspensions, Nat. Phys. Sci. 241 (105) (1973) 20–22.

[31] R.A. Spurr, H. Myers, Quantitative analysis of anatase-rutile mixtures with an X-Ray diffractometer, Anal. Chem. 29 (1957) 760–762, https://doi.org/10.1021/ac60125a006.

[32] J.R. Lombardi, R.L. Birke, A unified approach to surface-enhanced raman spectroscopy, J. Phys. Chem. C 112 (2008) 5605–5617, https://doi.org/10.1021/jp800167v.

[33] J. Yan, Y. Zhao, X. Wang, S. Xia, Y. Zhang, Y. Han, J. Yu, B. Ding, Polymer template synthesis of soft, light, and robust oxide ceramic films, Iscience. 15 (2019) 185–195.

[34] P. Pascariu, C. Cojocaru, P. Samoila, A. Airinei, N. Olaru, A. Rotaru, C. Romanitan, L.B. Tudoran, M. Suchea, Cu/TiO2 composite nanofibers with improved photocatalytic performance under UV and UV–visible light irradiation, Surf. Interfaces 28 (2022), 101644, https://doi.org/10.1016/j.surfin.2021.101644.

[35] S. Zhang, Y. Xu, W. Zhang, P. Cao, Synthesis, characterization, and photocatalytic performance of Cu/Y co-doped TiO2 nanoparticles, Mater. Chem. Phys. 277 (2022), 125558, https://doi.org/10.1016/j.matchemphys.2021.125558.

[36] J. Song, X. Wang, J. Yan, J. Yu, G. Sun, B. Ding, Soft Zr-doped TiO 2 nanofibrous membranes with enhanced photocatalytic activity for water purification, Sci. Rep. 7 (2017) 1–12.

[37] K. Okada, N. Yamamoto, Y. Kameshima, A. Yasumori, K.J.D. MacKenzie, Effect of silica additive on the anatase-to-rutile phase transition, J. Am. Ceram. Soc. 84 (2001) 1591–1596.

[38] R. Klaysri, S. Wichaidit, T. Tubchareon, S. Nokjan, S. Piticharoenphun, O. Mekasuwandumrong, P. Praserthdam, Impact of calcination atmospheres on the physiochemical and photocatalytic properties of nanocrystalline TiO2 and Si-doped TiO2, Ceram. Int. 41 (2015) 11409–11417, https://doi.org/10.1016/j.ceramint.2015.05.104.

[39] W. Wang, J. Zhou, S. Zhang, J. Song, H. Duan, M. Zhou, C. Gong, Z. Bao, B. Lu, X. Li, W. Lan, E. Xie, A novel method to fabricate silica nanotubes based on phase separation effect, J. Mater. Chem. 20 (41) (2010) 9068.

[40] S. Dong, B.M. Maciejewska, M. Lißner, D. Thomson, D. Townsend, R. Millar, N. Petrinic, N. Grobert, Unveiling the mechanism of the in situ formation of 3D fiber macroassemblies with controlled properties, ACS Nano 17 (7) (2023) 6800–6810.

[41] J. Turkevich, P.C. Stevenson, J. Hillier, A study of the nucleation and growth processes in the synthesis of colloidal gold, Discuss. Faraday Soc. 11 (1951) 55–75.

[42] X.-C. Ma, Y. Dai, L. Yu, B.-B. Huang, Energy transfer in plasmonic photocatalytic composites, Light Sci. Appl. 5 (2016) e16017–e.

[43] C. Clavero, Plasmon-induced hot-electron generation at nanoparticle/metal-oxide interfaces for photovoltaic and photocatalytic devices, Nat. Photonics 8 (2) (2014) 95–103.

[44] C. Peniche, D. Zaldívar, M. Pazos, S. Páz, A. Bulay, J.S. Román, Study of the thermal degradation of poly (N-vinyl-2-pyrrolidone) by thermogravimetry–FTIR, J. Appl. Polym. Sci. 50 (1993) 485–493.

[45] J. Zhang, J. Huang, X. Fang, Y. Li, Z. Yu, Z. Gao, S. Wu, L. Yang, J. Wu, J. Kui, Thermal decomposition and thermal reaction process of PTFE/Al/MnO2 fluorinated thermite, Materials (Basel). 11 (2018) 2451.

[46] R.I. Bickley, T. Gonzalez-Carreno, J.S. Lees, L. Palmisano, R.J.D. Tilley, A structural investigation of titanium dioxide photocatalysts, J. Solid State Chem. 92 (1991) 178–190, https://doi.org/10.1016/0022-4596(91)90255-G.

[47] D.C. Hurum, A.G. Agrios, K.A. Gray, T. Rajh, M.C. Thurnauer, Explaining the enhanced photocatalytic activity of degussa P25 Mixed-phase TiO2 using EPR, J. Phys. Chem. B 107 (2003) 4545–4549, https://doi.org/10.1021/jp0273934.

[48] F. Bensouici, M. Bououdina, A.A. Dakhel, R. Tala-Ighil, M. Tounane, A. Iratni, T. Souier, S. Liu, W. Cai, Optical, structural and photocatalysis properties of Cu-doped TiO2 thin films, Appl. Surf. Sci. 395 (2017) 110–116.

[49] B. Diffey, Solar spectral irradiance and summary outputs using excel, Photochem. Photobiol. 91 (2015) 553–557, https://doi.org/10.1111/php.12422.

[50] R. Bardestani, G.S. Patience, S. Kaliaguine, Experimental methods in chemical engineering: specific surface area and pore size distribution measurements—BET, BJH, and DFT, Can. J. Chem. Eng. 97 (2019) 2781–2791, https://doi.org/10.1002/cjce.23632.

[51] M.R. Ranade, A. Navrotsky, H.Z. Zhang, J.F. Banfield, S.H. Elder, A. Zaban, P. H. Borse, S.K. Kulkarni, G.S. Doran, H.J. Whitfield, Energetics of nanocrystalline TiO2, Proc. Natl. Acad. Sci. 99 (suppl_2) (2002) 6476–6481.

[52] J. V Alemán, A. V Chadwick, J. He, M. Hess, K. Horie, R.G. Jones, P. Kratochvíl, I. Meisel, I. Mita, G. Moad, Definitions of terms relating to the structure and processing of sols, gels, networks, and inorganic-organic hybrid materials (IUPAC Recommendations 2007), Pure Appl. Chem. 79 (2007) 1801–1829.

[53] J.G. Yu, H. Guo, S.A. Davis, S. Mann, Fabrication of hollow inorganic microspheres by chemically induced self-transformation, Adv. Funct. Mater. 16 (15) (2006) 2035–2041.

[54] Y. Yin, R.M. Rioux, C.K. Erdonmez, S. Hughes, G.A. Somorjai, A.P. Alivisatos, Formation of hollow nanocrystals through the nanoscale Kirkendall effect, Science (80-,) 304 (5671) (2004) 711–714.

[55] H.J. Fan, M. Knez, R. Scholz, D. Hesse, K. Nielsch, M. Zacharias, U. Gösele, Influence of surface diffusion on the formation of hollow nanostructures induced by the Kirkendall effect: the basic concept, Nano Lett. 7 (2007) 993–997.

[56] C.B.D. Marien, T. Cottineau, D. Robert, P. Drogui, TiO2 Nanotube arrays: Influence of tube length on the photocatalytic degradation of Paraquat, Appl. Catal. B Environ. 194 (2016) 1–6.

[57] Y. Yang, J. Wen, J. Wei, R. Xiong, J. Shi, C. Pan, Polypyrrole-decorated Ag-TiO2 nanofibers exhibiting enhanced photocatalytic activity under visible-light illumination, ACS Appl. Mater. Interfaces 5 (13) (2013) 6201–6207.

[58] N. Zhang, C. Han, Y.-J. Xu, J.J. Foley IV, D. Zhang, J. Codrington, S.K. Gray, Y. Sun, Near-field dielectric scattering promotes optical absorption by platinum nanoparticles, Nat. Photonics 10 (2016) 473–482.

[59] Y. Wen, B. Liu, W. Zeng, Y. Wang, Plasmonic photocatalysis properties of Au nanoparticles precipitated anatase/rutile mixed TiO 2 nanotubes, Nanoscale 5 (2013) 9739–9746.

[60] A. Zwijnenburg, A. Goossens, W.G. Sloof, M.W.J. Crajé, A.M. van der Kraan, L. Jos de Jongh, M. Makkee, J.A. Moulijn, XPS and Mössbauer characterization of Au/TiO2 propene epoxidation catalysts, J. Phys. Chem. B 106 (38) (2002) 9853–9862.

[61] L.K. Ono, D. Sudfeld, B. Roldan Cuenya, In situ gas-phase catalytic properties of TiC-supported size-selected gold nanoparticles synthesized by diblock copolymer encapsulation, Surf. Sci. 600 (23) (2006) 5041–5050.

[62] Z. Jiang, W. Zhang, L.i. Jin, X. Yang, F. Xu, J. Zhu, W. Huang, Direct XPS evidence for charge transfer from a reduced rutile TiO2 (110) surface to Au clusters, J. Phys. Chem. C 111 (33) (2007) 12434–12439.

[63] Y. Li, X. Li, J. Li, J. Yin, Photocatalytic degradation of methyl orange by TiO2-coated activated carbon and kinetic study, Water Res. 40 (2006) 1119–1126, https://doi.org/10.1016/j.watres.2005.12.042.

[64] M.-C. Wu, P.-H. Lee, D.-L. Lee, Enhanced photocatalytic activity of palladium decorated TiO2 nanofibers containing anatase-rutile mixed phase, Int. J. Hydrogen Energy 40 (2015) 4558–4566.

[65] A. Houas, H. Lachheb, M. Ksibi, E. Elaloui, C. Guillard, J.-M. Herrmann, Photocatalytic degradation pathway of methylene blue in water, Appl. Catal. B Environ. 31 (2001) 145–157, https://doi.org/10.1016/S0926-3373(00)00276-9.

[66] J. Gamage McEvoy, W. Cui, Z. Zhang, Degradative and disinfective properties of carbon-doped anatase–rutile TiO2 mixtures under visible light irradiation, Catal. Today. 207 (2013) 191–199. https://doi.org/https://doi.org/10.1016/j.cattod.2012.04.015.

[67] X. Yang, V. Salles, M. Maillard, Y.V. Kaneti, M. Liu, C. Journet, X. Jiang, Y. Liu, A. Brioude, Fabrication of Au functionalized TiO2 nanofibers for photocatalytic application, J. Nanoparticle Res. 21 (2019) 160, https://doi.org/10.1007/s11051-019-4600-8.

[68] M.J. Nalbandian, K.E. Greenstein, D. Shuai, M. Zhang, Y.-H. Choa, G.F. Parkin, N. V. Myung, D.M. Cwiertny, Tailored synthesis of photoactive TiO2 nanofibers and Au/TiO2 nanofiber composites: structure and reactivity optimization for water treatment applications, Environ. Sci. Tech. 49 (2015) 1654–1663.
[69] S.T. Kochuveedu, D.-P. Kim, D.H. Kim, Surface-plasmon-induced visible light photocatalytic activity of TiO2 nanospheres decorated by Au nanoparticles with controlled configuration, J. Phys. Chem. C 116 (3) (2012) 2500–2506.
[70] Y. Cheng, J. Gao, Q. Shi, Z. Li, W. Huang, In situ electrochemical reduced Au loaded black TiO2 nanotubes for visible light photocatalysis, J. Alloy. Compd. 901 (2022), 163562, https://doi.org/10.1016/j.jallcom.2021.163562.
[71] T. Wei, J. Xu, C. Kan, L. Zhang, X. Zhu, Au tailored on g-C3N4/TiO2 heterostructure for enhanced photocatalytic performance, J. Alloy. Compd. 894 (2022), 162338, https://doi.org/10.1016/j.jallcom.2021.162338.
[72] S.M. Tichapondwa, J.P. Newman, O. Kubheka, Effect of TiO2 phase on the photocatalytic degradation of methylene blue dye, Phys. Chem. Earth, Parts A/B/C. 118 (2020), 102900.